Out-of-plane quadrupolar excitons in Ruddlesden-Popper perovskites: theoretical insights into effects of organic spacer cations

Journal:	*Materials Horizons*
Manuscript ID	MH-COM-01-2025-000166.R1
Article Type:	Communication
Date Submitted by the Author:	27-Apr-2025
Complete List of Authors:	Feng, Qingjie; Zhejiang Normal University Department of Physics Zhang, Xu; California State University Northridge, Department of Physics and Astronomy Nan, Guangjun; Zhejiang Normal University, Department of Physics

New concepts

Owing to strong quantum and dielectric confinement, two-dimensional (2D) Ruddlesden-Popper perovskites (RPPs) offer a valuable playground for studying excitonic properties in particular considering that the organic spacer cations can largely complicate the nature of band-edge carriers. While exciton fine structure was recently assigned by theoretical atomistic simulations with ab-initio many-body electronic structure approaches, the organic spacer cations were replaced by Cs species, leading the effects of organic spacer cations on excitons in 2D RPPs to be excluded. In this study, the density functional theory and a newly developed time-dependent density functional theory approaches are adopted to investigate excitonic characteristics of 2D RPPs. Strikingly, the out-of-plane quadrupolar characteristic of excitons is demonstrated in the inorganic sublattice which is attributed to the hydrogen bonding between organic spacer cations and apical I ions of inorganic octahedron. Besides, the correlation between the quadrupole of exciton and dipoles of organic species is unveiled, providing for the first time a complete picture for the roles of organic spacer cations on exciton states in 2D RPPs. The existence of the quadrupolar excitons in 2D RPPs provides a new strategy to produce the quadrupolar excitons without the needs of the multilayered structures like transition metal dichalcogenide heterotrilayers.

Out-of-plane quadrupolar excitons in Ruddlesden-Popper perovskites: theoretical insights into effects of organic spacer cations

Qingjie Feng[1], Xu Zhang[2,*], Guangjun Nan[1,*]

[1] Department of Physics, Zhejiang Normal University, Jinhua, Zhejiang 321004, P. R. China

[2] Department of Physics and Astronomy, California State University Northridge, Northridge, California 91330-8268, United States

*Corresponding authors: E-mail: xu.zhang@csun.edu; gjnan@zjnu.edu.cn

Abstract

Two-dimensional (2D) Ruddlesden-Popper perovskites (RPPs), a kind of semiconductor materials with strong quantum and dielectric confinement, offer a valuable platform for studying excitonic properties. However, the effects of organic spacer cations on excitons in 2D RPPs have not been elucidated to date, impeding the understanding for the nature of excitons and relevant physics behind the excitons in 2D RPPs. Herein, the excitonic properties in 2D RPPs which consist of organic and inorganic sublattices are assessed by adopting density functional theory and time-dependent density functional theory approaches. Strikingly, the out-of-plane (OP) quadrupolar characteristic of excitons is demonstrated in the inorganic sublattice – wherein the electron densities are confined in equatorial Pb-I layers sandwiched by the top and bottom apical I layers in presence of partial hole densities. Given that the oscillator strength of in-plane exciton is one order of magnitude larger than that of OP exciton, the OP quadrupolar charge distribution is mainly contributed by the in-plane exciton. The origin of the quadrupolar polarization of excitons is attributed to the hydrogen bonding between organic spacer cations and apical I ions of inorganic octahedron, which are sensitively determined by the dipolar nature of the organic spacer cations. Finally, the differences of the quadrupolar excitons between 2D RPPs and transition metal dichalcogenide trilayer heterostructures are discussed in this work.

1. Introduction

Hybrid organic-inorganic perovskites have garnered significant attention in recent years due to their wild synthetic condition and unique optoelectronic properties.[1] The combination of factors makes them as promising semiconducting materials for optoelectronic applications, including solar cells,[2] light-emitting diodes,[3] lasers[4] and photodetectors.[5] Relative to three-dimensional counterparts, two-dimensional (2D) hybrid perovskites represent a fascinating alternative thanks to their enhanced moisture stability and larger degrees of structural freedom.[6] 2D Ruddlesden-Popper perovskites (RPPs) possess atomically thin inorganic quantum well layers sandwiched between electronically inert organic spacer cations which are linked to inorganic octahedra through hydrogen bonding between ammonium groups and halogen anions.[7] Such 2D layered structures produce strong quantum and dielectric confinement, leading their optical properties to be often driven by excitons – a quasi-particle composed of a photogenerated electron and hole pair bound by Coulomb attraction.[8] Thereby, 2D RPPs offer a valuable playground for studying excitonic properties in particular considering that the organic spacer cations, which are absent in inorganic single-layer systems such as transition metal dichalcogenides (TMDs) and their inorganic analogous, can largely complicate the nature of band-edge carriers.[9, 10]

In an exciton, spins of electron and hole can be either parallel or antiparallel. The optical transition is spin-forbidden for the exciton with an antiparallel spin arrangement, which is termed a dark exciton (X_D). By contrast, the electron-hole (e-h) recombination by emitting light is optically active for the exciton with a parallel spin arrangement, which is referred to as a bright exciton (X_B). In 2D RPPs with low lattice symmetry, enhanced exchange interactions between electron and hole carriers completely lift degeneracy of X_B states.[11] This gives rise to two bright excitonic states with the transition dipole moment confining in the plane of inorganic flake and one bright excitonic state with the transition dipole polarization oriented along the out-of-plane direction of the inorganic sheet,[12] which is defined as in-plane (IP) and out-of-plane (OP) excitonic states, respectively. Considering that the OP excitonic states are often missing in “classical” inorganic single-layer materials, such as TMDs which sustain excitons with intrinsic IP electric dipole polarization,[13-15] the presence of excitons with OP electric dipole polarization in 2D RPPs, like the archetypal $(PEA)_2PbI_4$ with PEA standing for phenylethylammonium,[16] is even more intriguing.[12, 17, 18] This is because the OP excitons can potentially enable 2D RPPs for the emerging applications in integrated photonic chips with the needs of OP electric dipole orientation.[14, 19] Unfortunately, the physics behind the formation of the OP excitons has yet been clarified to date.

Very recently, experimental studies reached a consensus for low-energy exciton states: (i) the dark state is positioned below the bright states;[20, 21] (ii) the energy of OP excitonic state is higher than those of IP excitonic states.[11, 12, 22, 23] The excitonic-level assignment was subsequently corroborated by theoretical atomistic simulations with ab-initio many-body electronic structure approaches,[24] but the organic space cations were substituted by Cs species, leading the effects of organic spacer cations on excitons in 2D RPPs to be excluded. As a matter of fact, the choice of organic spacer cations was demonstrated to impact dielectric environment, bandgap energy and distortion of inorganic octahedral units.[25-28] More importantly, the single-particle energy levels of organic species, which are expected to be deeply buried below the valence band edge (VBE) contributed by the inorganic framework when organic and inorganic sublattices are isolated,[29] are promoted to the VBE of 2D RPPs owing to the interplays between inorganic networks and organic spacer layers.[30, 31] Resultantly, the dark-bright excitonic-level splitting and the nature of exciton states in 2D RPPs might be nontrivially affected by the choice of organic spacer cations.[32, 33]

Here, by means of density functional theory (DFT) and time-dependent density functional theory (TDDFT) approaches, we address the effects of organic spacer cations on the exciton states by focusing on $(PEA)_2(MA)_{n-1}Pb_nI_{3n+1}$ RPPs (MA = CH_3NH_3) with different *n* values. It is strikingly found that (i) both IP and OP excitons display similar quadrupolar charge distribution in the inorganic sublattice – wherein the electron densities are confined in equatorial Pb-I layers sandwiched by the top and bottom apical I layers while partial hole densities are situated in the two apical I layers; (ii) due to the quadrupolar characteristic, both IP and OP excitons have the OP electric dipole polarization when the structural symmetry is broken due to the thermal fluctuation. Considering that the oscillator strength of IP exciton is one order of magnitude larger than that of OP exciton, the OP electric dipole polarization in 2D RPPs is predominantly contributed by the IP excitons. When projecting these exciton states onto the single-particle energy levels, the OP quadrupolar characteristic of excitons is unambiguously ascribed to the interplays between organic spacer cations and apical I ions at the outermost of inorganic sublattices. Besides, the correlation between the quadrupole of exciton and dipoles of organic species is unveiled. This study provides for the first time a complete picture for the roles of organic spacer cations on the exciton states in 2D RPPs.

2. Computational details

In this study, two crystalline phases of $(PEA)_2(MA)_{n-1}Pb_nI_{3n+1}$ RPPs are chosen with their structures shown in the following section. Specifically, one phase exhibits the primitive cell with the incorporation of a quantum well layer[34] and the other phase holds two inorganic layers in the primitive cell with Pb species in a sheet centered on the inorganic cavities of the neighboring sheet.[35, 36] For convenience below, the former phase and the latter phase is defined as $(PEA)_2(MA)_{n-1}Pb_nI_{3n+1}$-(1) and

$(PEA)_2(MA)_{n-1}Pb_nI_{3n+1}$-(2), respectively.

According to the experimentally resolved lattice parameters, the ground-state geometries are optimized by using the DFT method, which could be implemented with the Vienna ab initio simulation package.[37] The projected-augmented wave pseudopotential and Perdew−Burke−Ernzerhof functional is employed to treat electron-nucleus interactions and exchange-correlation effect, respectively.[38, 39] For Pb, I, C, N, and H species, the number of considered valence electrons is 4, 7, 4, 5, and 1, respectively. The electron wavefunctions are described by using the plane-wave basis set with the cutoff energy of 400 eV. The convergence criterion of Hellman–Feynman forces and total energy is set as 10^{-2} eV/Å and 10^{-5} eV, respectively. The Brillouin zone is sampled by adopting a 5 ◊ 5 ◊ 1 Monkhorst-Pack *k*-point mesh. Moreover, the semiempirical DFT-D2 method is adopted to deal with the van der Waals interactions in the 2D RPPs.[40] The high-frequency dielectric constant is evaluated with the aid of the approach by Gajdoš *et al* [41] and the DOS is calculated by adopting HSE06 (α=0.43) functional with SOC corrections. Subsequently, the supercells are generated by considering a 2 × 2 × 1 periodicity for each crystalline phase. Owing to the large size of the supercells, the geometric relaxation is performed by sampling the Brillouin zone at Γ point. Then the ab initio molecular dynamics simulation is carried out by increasing the temperature to 300 K with repeated velocity scaling. Subsequently, the ab initio molecular dynamics run with a time-step of 1 fs at 300 K is performed by keeping the canonical ensemble with the Nosé-Hoover thermostat. The geometric structures after 2 ps (Figure S1) are selected to investigate excitonic states. Notably, excitonic characteristics including excitonic levels, oscillator strengths and photoexcited e-h densities are assessed by applying a newly developed TDDFT approach which is in the framework of linear response theory.[42] This TDDFT scheme is implemented in conjunction with an optimally tuned, screened and range-separated hybrid (OT-SRSH) functional,[43-45] which can also treat the SOC effect when formulating with spinor wavefunction.[46] More details for the TDDFT formalism included in an in-house code are provided in the Supplementary Information.

3. Results and discussion

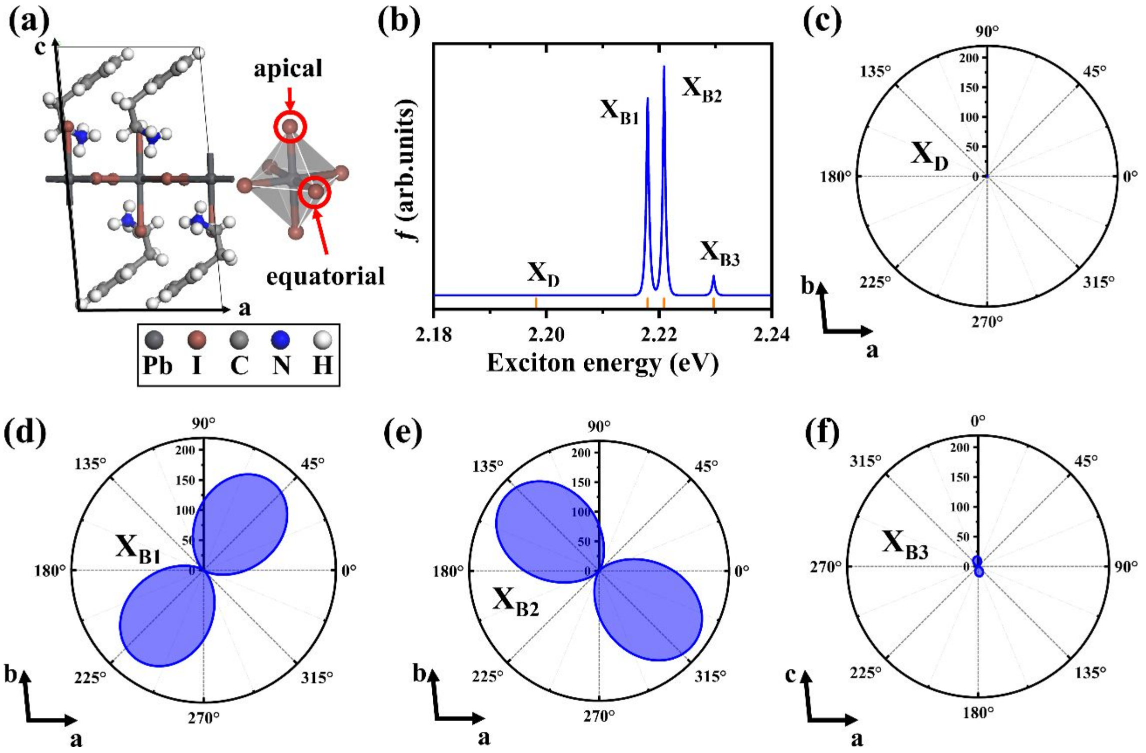

Figure 1. Excitonic properties of $(PEA)_2PbI_4$-(1) phase in DFT-relaxed ground-state geometries. (a) Structure of $(PEA)_2PbI_4$-(1) phase with the denotion of I species at apical and equatorial positions. (b) Exciton oscillator strength (*f*) with orange bars representing excitonic energy levels of dark state (X_D) and bright states (X_{B1} and X_{B2} for IP exciton states as well as X_{B3} for OP exciton state). (c-f) The oscillator strength of X_D, X_{B1}, X_{B2} and X_{B3} exciton states as a function of transition dipole polarization direction, respectively.

We start our discussion by analyzing exciton fine structure according to the relaxed ground-state geometries of the $(PEA)_2PbI_4$-(1) phase (Figure 1a). Based on the excitonic energy levels and associated oscillator strengths (Figure 1b), it is found that (i) the X_D state (Figure 1c) locates ~22 meV below the IP X_B states, which is comparable to the values reported by experiments at cryogenic temperature;[23, 47, 48] (ii) The energy splitting is ~2 meV between the two IP X_B states with their dipole polarizations to be orthogonally oriented (Figures 1d and 1e), fully in line with the experimental results;[11, 49, 50] (iii) Compared to IP excitonic states, the OP bright excitonic state exhibits much weaker oscillator strength (Figure 1f), which matches the weak signals of OP excitonic states in experiments.[18, 51]

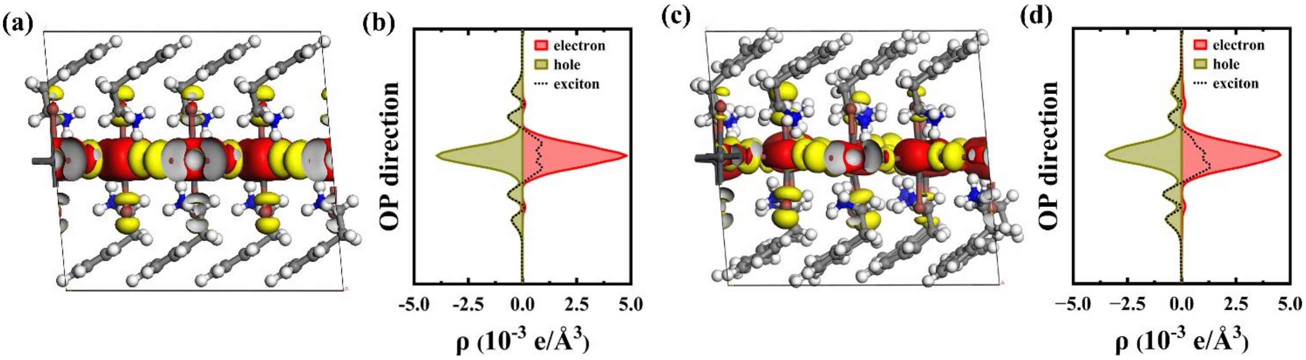

Figure 2. Exciton distributions in $(PEA)_2PbI_4$-(1) phase. (a) Exciton distributions for one of the studied exciton states in DFT-relaxed 3D lattice. (b) Light-triggered electron and hole densities (shaded regions) as well as the corresponding exciton densities along the OP direction (dotted line) according to the geometries in (a). (c) Exciton distributions for one of the studied exciton states in 3D lattice at one snapshot during dynamical simulation at 300 K. (d) Photoexcited electron and hole densities (shaded regions) as well as the corresponding exciton densities with quadrupolar characteristic along the OP direction (dotted line) according to the geometries in (c). The positive (negative) values in horizontal coordinate of (b) and (d) denote electron (hole) densities in (a) and (c) with the iso-surface

value being 1.0×10^{-3} e/Å^3.

Charge densities of these exciton states are then scrutinized. Very surprisingly, all the studied exciton states exhibit similar charge distributions (Figure S2), one of which is shown in Figure 2a. When decomposing the exciton into hole and electron (Figure 2b), it is found that both hole and electron densities are symmetrically located with respect to the Pb-I layers with most of electron and hole densities being confined in the inorganic sheet. When the temperature effect is taken into account, the symmetric charge distributions with respect to the Pb-I layers turn to be asymmetric due to the breaking of the structural symmetry (Figure 2c), leading a fraction of hole to reside asymmetrically on the top and bottom apical I layers sandwiching the Pb-I layers (Figure 2d). In other word, an asymmetric quadrupolar characteristic of exciton along the OP direction is formed in the inorganic sublattice, resulting in the OP electric dipole polarization. Similar to the case in relaxed ground-state structure (Figure 1), the oscillator strengths of IP excitonic states are one order of magnitude larger than that of OP excitonic state (Figure S3) for the geometries at the selected snapshot. This means that the OP electric dipole polarization should predominantly stem from the IP excitons when all the bright exciton states are optically accessible. This is in sharp contrast to the postulation in literature that the OP electric dipole polarization only originates from the OP excitons.[12, 18]

The transition amplitude analysis from occupied single-particle orbitals to unoccupied single-particle orbitals is critical towards correlating the exciton states with the single-particle DOS. According to the transition amplitudes (Figure S2), the optical excitation of studied exciton states mainly results from electron transition from VBE and VBE – 1 levels to conduction band edge (CBE) and CBE + 1 levels. Note that it is energetically degenerate for VBE and VBE – 1 levels as well as for

CBM and CBM + 1 levels, the optical excitation is overwhelmingly determined by the single-particle orbitals at band edges. Since the OT-SRSH functionals adopted in this work do not impact the relative magnitude of the DOS from different compositions of $(PEA)_2PbI_4$-(1) material (Figure S4), the partial DOS calculated at HSE06+SOC level of theory is shown in Figure 3. In line with other theoretical calculations,[52] the CBE is largely composed of Pb species and the VBE is predominantly made up of Pb and I species (Figure 3a). Herein, it is worth stressing that (i) the CBE is dominantly contributed by the p_x and p_y orbitals of Pb species (Figures 3b and S5) which confine the electron to the in-plane of inorganic sheet; (ii) In addition to the s orbitals of Pb species, the VBE is also contributed by the p_x and p_y orbitals of I species at equatorial site (Figures 3c and S6) and the p_z orbitals of I species at apical position (Figures 3d and S6), thereby driving the hole to be confined on Pb ions as well as I ions at both equatorial and apical sites. Thus, the hole densities distribute on all the three layers (namely one Pb-I layer sandwiched by two sheets consisting of the I ions at the apical site) of the inorganic flake, which causes the OP quadrupolar characteristic of excitons. It is concluded that the existence of OP quadrupole in 2D RPPs is due to the fact that the VBE originates from both the equatorial and apical I species with their IP (p_x and p_y) and OP (p_z) orbitals, respectively. Such conclusion is demonstrated to be little affected by the sizes of the adopted models even if the Brillouin zone is sampled with different *k*-point meshes (Figure S7).

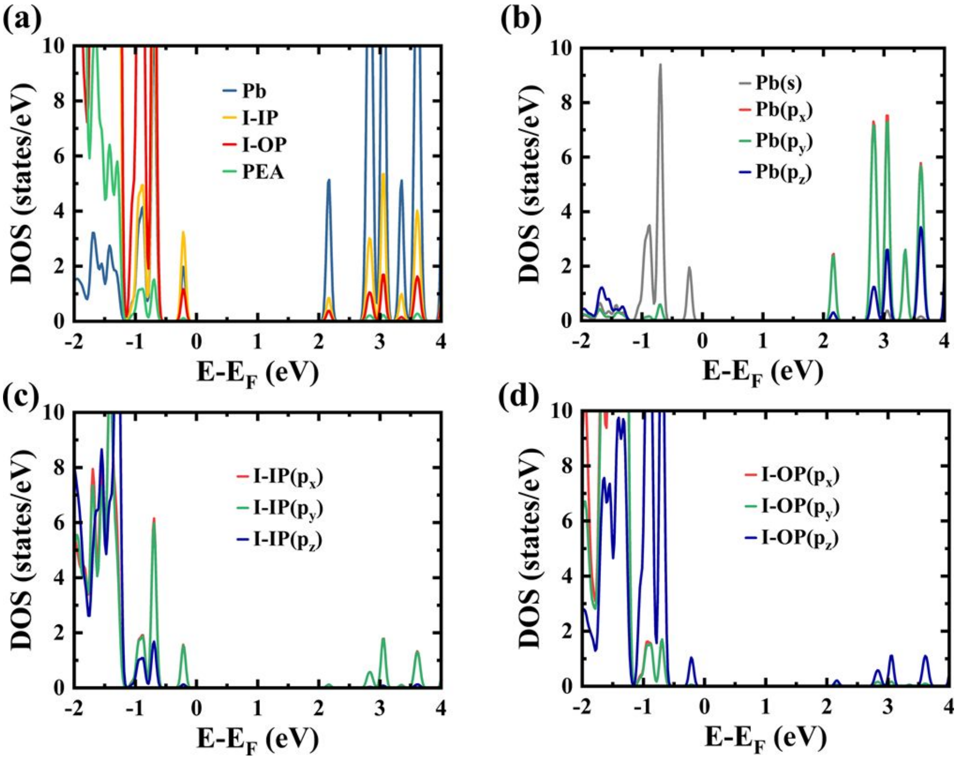

Figure 3. DOS of $(PEA)_2PbI_4$-(1) phase calculated at HSE06+SOC level of theory. (a) DOS for Pb ions, equatorial I ions (I-IP), apical I ions (I-OP) and PEA cations. (b) Partial DOS resulting from s, p_x, p_y and p_z orbitals of Pb species. (c) Partial DOS for p_x, p_y and p_z orbitals of I species at the equatorial site. (d) Partial DOS for p_x, p_y and p_z orbitals of apical I species.

Next, we examine the dependence of OP quadrupole on the thickness of inorganic sublattice. It is found that the OP exciton gets weakened with the increase of *n* values (Figures 2b, S8b and S8h). This is rationalized by analyzing the DOS of equatorial and apical I species for $(PEA)_2(MA)Pb_2I_7$-(1) and $(PEA)_2(MA)_2Pb_3I_{10}$-(1) which are shown in Figure S8. By comparing the VBEs of the $(PEA)_2(MA)_{n-1}Pb_nI_{3n+1}$-(1) as a function of n (n = 1, 2 and 3), it is noticed that the DOS of the apical I ions locating at the outermost of inorganic sublattice diminishes monotonically with *n* values (Figure 4a). Here, we use η to quantify the strength of OP quadrupole, which is defined as the ratio of OP exciton charge densities over the total exciton charge densities. It is found that η reduces with *n* values (Figure 4a). These results suggest that the OP quadrupole is positively correlated with the DOS of the apical I species at the outermost of inorganic sublattice. Given the fact that excitons are embedded in a background consisting of 2D inorganic layers with a relatively high dielectric surrounded by organic layers with a lower dielectric,[53] the trends with *n* values in Figure 4a are plausibly associated to the change of dielectric screening with *n* values (Figure 4b). Specifically, the dielectric screening is weakened particularly along OP direction as the inorganic layer thickness reduces (Figure 4b).

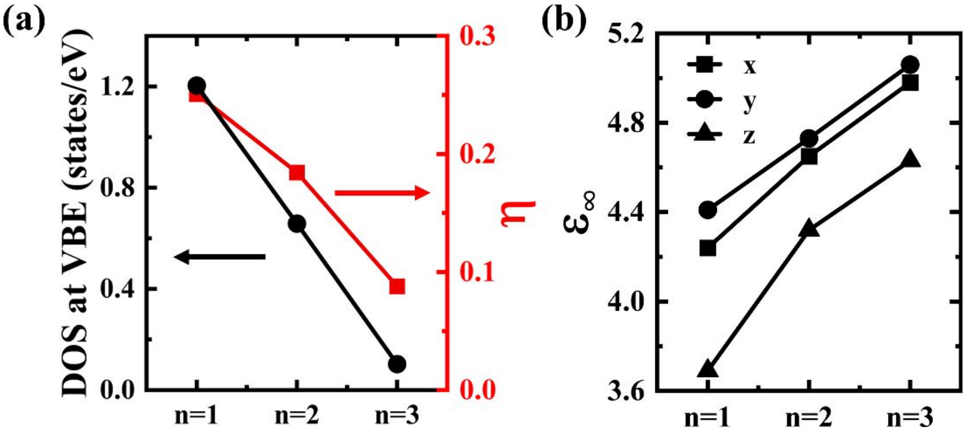

Figure 4. Electronic and excitonic properties as a function of dielectric screening in $(PEA)_2(MA)_{n-1}Pb_nI_{3n+1}$-(1) (*n* = 1, 2 and 3) RPPs. (a) DOS at VBE for apical I ions at the outermost of inorganic sublattice and η. (b) High-frequency dielectric constant (ε_∞) along IP (x and y) and OP (z) directions.

Considering the interplays between inorganic and organic sublattices,[30, 54, 55] it is reasonably proposed that the decrease of the p_z orbitals at VBEs with *n* values (Figure 4a) is due to the weakening of the electronic interactions at the organic/inorganic interfaces of $(PEA)_2(MA)_{n-1}Pb_nI_{3n+1}$ RPPs. To corroborate this hypothesis, the adopted $(PEA)_2PbI_4$-(1) structure (Figure 1a) is stretched along the OP direction by moving the organic layers 1 Å away from the inorganic framework (Figure 5a), which has been demonstrated to effectively reduce the interactions between inorganic and organic sublattices.[31] Indeed, the DOS at VBE for the apical I ions in the stretched $(PEA)_2PbI_4$-(1) (Figure 5b) decrease 19.0% with respect to the unstretched case (Figure 3a), resulting in the ratio of OP exciton densities to decrease 19.7% (Figure 5c) although the oscillator strengths of each of the bright exciton states are slightly changed (Figure S9). Thereby, it can be concluded that the interactions between inorganic and organic sublattices trigger the p_z orbital of apical I ions in $(PEA)_2PbI_4$-(1) to be involved into the VBE. Interestingly, the electron-vibration interactions were found to be dominated by the movement of the iodine ions at the apical site,[56] which might be related to the electronic coupling at the organic/inorganic interfaces. The increased thickness of inorganic framework results in larger dielectric screening and thus reduced organic/inorganic electronic interactions, leading to the decrease of OP quadrupole.

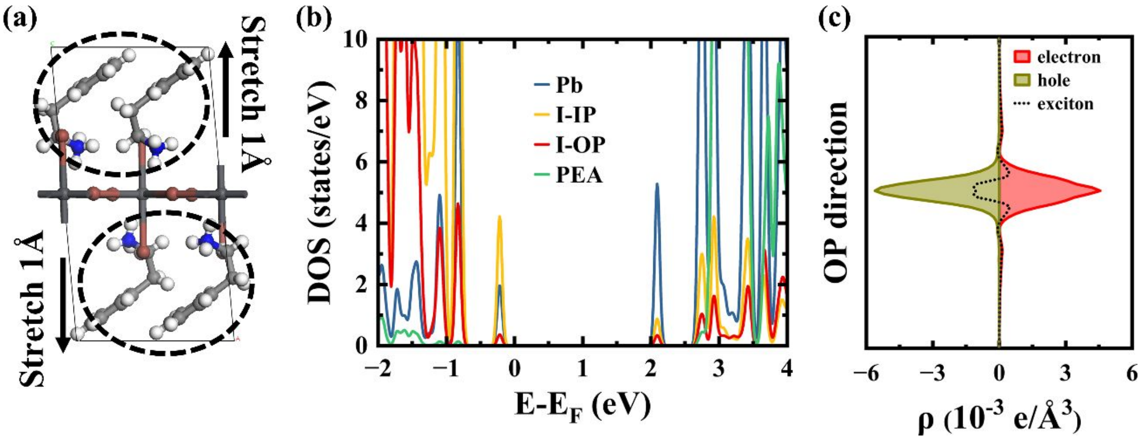

Figure 5. Electronic and excitonic properties for the stretched $(PEA)_2PbI_4$-(1) structure. (a) Schematics for stretching the $(PEA)_2PbI_4$-(1) structure. (b) Partial DOS for Pb species, equatorial I species, apical I species and organic spacer species. (c) Photogenerated electron and hole densities (shaded regions)

as well as exciton densities along the OP direction (dotted line) for any one of the studied exciton states.

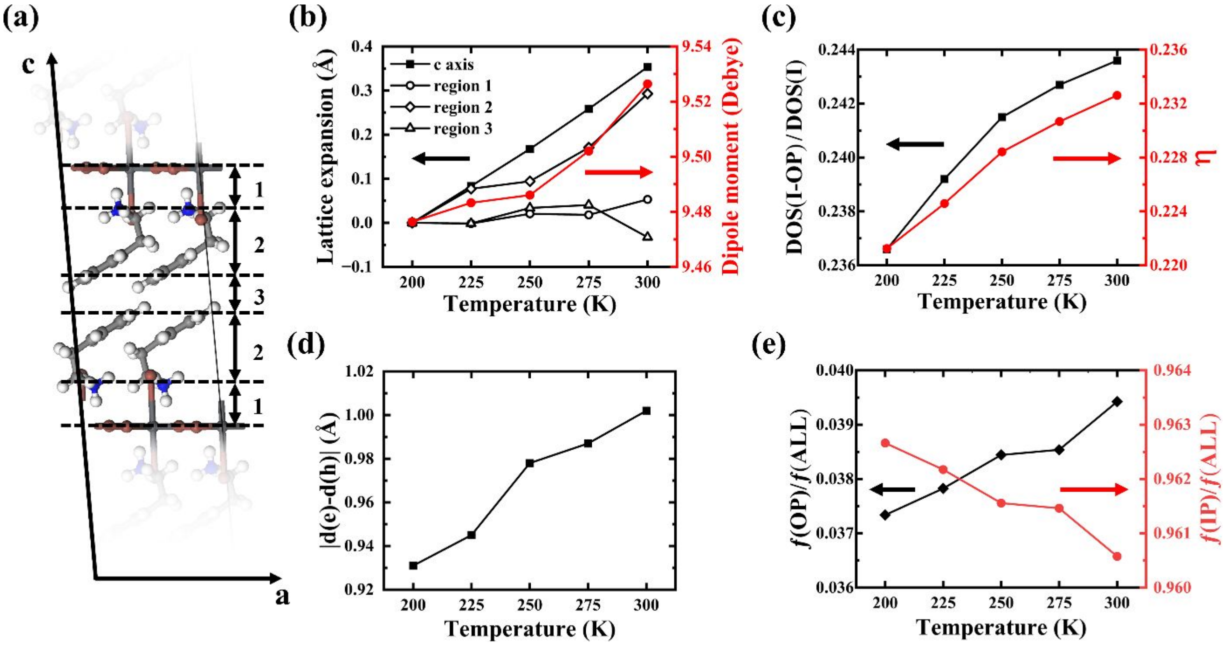

Figure 6. The change of lattice parameters of $(PEA)_2PbI_4$-(2) phase for the influence of electronic and excitonic properties. (a) Structure of $(PEA)_2PbI_4$-(2) phase. (b) Lattice expansion along *c* axis for the experimentally reported primitive cells with temperature. The change of the region 1-3 defined in (a) and the calculated dipole moments of PEA cations are also presented. (c) DOS(I-OP)/DOS(I) (ratios of DOS of apical I species over DOS of all the I species at VBE) and η as a function of the experimentally reported lattices at different temperatures. (d) Effective e-h distance along the OP direction as a function of the experimentally reported lattices at different temperatures. (e) Ratios of oscillator strengths of OP and IP bright states over all the bright exciton states.

Lastly, we find that the oscillator strength of IP/OP bright excitons and the quadrupolar polarization sensitively depend on the temperature. Experiments show that the lattice parameters of the $(PEA)_2PbI_4$-(2) phase (Figure 6a) increase considerably along the c axis with respect to the negligible lattice expansion in a-b plane with temperature (Figures S10 and 6b).[36] Interestingly, the contribution of apical I species for the VBE, which is quantified by calculating the ratios of DOS of apical I species over DOS of all the I species, increases monotonically with lattice expansion (Figure 6c). Besides, the contribution of apical I ions for the VBE is always positively related to the strength of OP quadrupole (Figure 6c). Following the definition of electron (or hole) position $d = \left(\sum_i z\rho_i(z)\right)/\left(\sum_i \rho_i(z)\right)$ with $\rho(z)$ representing the electron (or hole) densities at a specific coordinate z along the OP direction, the effective distance between the electron in the Pb-I layer and the hole in the top (or bottom) apical I layer is found to increase monotonically with the lattice expansion (Figure 6d). To understand these variations in Figures 6c and 6d, we decompose the primitive cell along c axis into three regions (Figure 6a). It is found that the region 2, which represents the length of PEA cations along c axis, exhibits the most prominent expansion along c axis for the lattices at various temperatures (Figure 6b). Resultantly, the dipole moment of PEA cations increases with the expansion of region 2 (Figure 6b). Since the contributions of apical I species for the DOS at VBE have been ascribed to the organic/inorganic electronic interactions, it is anticipated that such interactions at organic/inorganic interfaces are proportionally relied on the dipole moment of PEA cations. Such anticipation is further supported by the ground-state energy differences between the unstretched and stretched structures which increase monotonically with lattice expansion along c axis (Figure S11). This is because the organic/inorganic interactions, if stronger, are expected to decay increasingly faster with interfacial distance, given that organic spacer cations interplay with inorganic octahedra through hydrogen bonding.[7] Correspondingly, the DOS of apical I species at VBE decreases increasingly with lattice expansion along the c axis (Figure S11). This implies that the incorporation of fluorine species into the organic spacers which could increase the dipoles of organic species could be feasible to manipulate the OP exciton fraction.[57] Besides, it is worth noting that the oscillator strengths of the IP (OP) bright states are inversely (positively) proportional to the organic/inorganic interactions in $(PEA)_2PbI_4$ material (Figure 6e). These provides an unprecedented opportunity to modulate the magnitude of IP and OP transition dipole polarization by changing the structures of organic spacers.

Recently, the quadrupolar excitons have been experimentally observed in TMD heterotrilayers.[58-60] Herein, it is worth stressing that the mechanism of the formation of the quadrupolar excitons in TMD heterotrilayers is different from the case in 2D RPPs. In TMD heterotrilayers, the emergence of the quadrupolar excitons is a consequence of the assembled monolayers by the van der Waal force. According to the chemical compositions of the TMD monolayers, the electron (hole) can manageably reside in the middle (top and bottom) sheet of TMD heterotrilayers and vice versa. By contrast, despite the 2D RPPs have a trilayer heterostructure with the inorganic layer sandwiched by the top and bottom organic spacer layers (Figure 1a), the quadrupolar excitons are confined within the inorganic layer displaying the partial hole occupation on the apical I layers which sandwich the inorganic Pb-I layer with the electron occupation. In addition, the formation of the quadrupolar excitons in 2D RPPs is triggered by the hydrogen bonding between the inorganic framework and the organic spacer layers, which is affected by the electrostatic interaction between the dipoles of the organic spacer cations and I p_z orbitals. The existence of the quadrupolar excitons in 2D RPPs provides a new strategy to produce the quadrupolar excitons without the needs of the multilayered structures like the TMD heterotrilayers. More interestingly, the quadrupolar excitons can be tuned by the thickness of inorganic flake.

4. Conclusions

In conclusion, this work combines DFT and TDDFT approaches to provide theoretical insights for the effects of organic spacer cations on excitonic properties of the $(PEA)_2(MA)_{n-1}Pb_nI_{3n+1}$ materials. Compared to the recent assignment of the exciton fine structure reported by experiments and theoretical calculations, the organic species are found to have marginal influence for the exciton fine structure. Nevertheless, it is surprisingly found that the IP exciton states predominantly contribute OP quadrupolar characteristic which consistently displays electron densities residing in the Pb-I layers sandwiched by the top and bottom apical I layers with the location of partial hole densities. The reason is unambiguously attributed to the interplays between organic spacer cations and I ions at the apical site of inorganic octahedron, which is a consequence of weak electrostatic screening along the OP direction. Besides, the dipole moments of the organic species are found to sensitively determine the electronic interactions between inorganic and organic sublattices, which in turn affect the strength of OP quadrupole. Our demonstration identifies the effects of organic spacer cations on the excitons, paving the way towards rational design of 2D RPPs with tailored properties of OP quadrupolar excitons and beyond.

Author contributions

Q. Feng: investigation, visualization, and writing – original draft. X. Zhang: methodology and software. G. Nan: conceptualization, supervision, and writing – review & editing.

Conflicts of interest

There are no conflicts to declare.

Acknowledgments

G.N. acknowledges the National Natural Science Foundation of China (Grant No. 22273088). X.Z. acknowledges the U.S. National Science Foundation (Grants DMR-2105918).

References

1. I. Metcalf, S. Sidhik, H. Zhang, A. Agrawal, J. Persaud, J. Hou, J. Even and A. D. Mohite, *Chem. Rev.*, 2023, **123**, 9565-9652.
2. A. K. Jena, A. Kulkarni and T. Miyasaka, *Chem. Rev.*, 2019, **119**, 3036-3103.
3. M. Lu, Y. Zhang, S. Wang, J. Guo, W. W. Yu and A. L. Rogach, *Adv. Funct. Mater.*, 2019, **29**, 1902008.
4. Q. Zhang, Q. Shang, R. Su, T. T. H. Do and Q. Xiong, *Nano Lett.*, 2021, **21**, 1903-1914.
5. P. Wangyang, C. Gong, G. Rao, K. Hu, X. Wang, C. Yan, L. Dai, C. Wu and J. Xiong, *Adv. Opt. Mater.*, 2018, **6**, 1701302.
6. G. Grancini and M. K. Nazeeruddin, *Nat. Rev. Mater.*, 2019, **4**, 4-22.
7. M. P. Arciniegas and L. Manna, *ACS Energy Lett.*, 2022, **7**, 2944-2953.
8. Y. Chen, Y. Sun, J. Peng, J. Tang, K. Zheng and Z. Liang, *Adv. Mater.*, 2018, **30**, 1703487.
9. C. J. Dahlman, R. M. Kennard, P. Paluch, N. R. Venkatesan, M. L. Chabinyc and G. N. Manjunatha Reddy, *Chem. Mater.*, 2021, **33**, 642-656.
10. H. Ren, S. Yu, L. Chao, Y. Xia, Y. Sun, S. Zuo, F. Li, T. Niu, Y. Yang, H. Ju, B. Li, H. Du, X. Gao, J. Zhang, J. Wang, L. Zhang, Y. Chen and W. Huang, *Nat. Photonics*, 2020, **14**, 154-163.
11. T. T. H. Do, A. Granados del Águila, D. Zhang, J. Xing, S. Liu, M. A. Prosnikov, W. Gao, K. Chang, P. C. M. Christianen and Q. Xiong, *Nano Lett.*, 2020, **20**, 5141-5148.
12. K. Posmyk, M. Dyksik, A. Surrente, D. K. Maude, N. Zawadzka, A. Babiński, M. R. Molas, W.

Paritmongkol, M. Mączka, W. A. Tisdale, P. Plochocka and M. Baranowski, *Adv. Opt. Mater.*, 2024, **12**, 2300877.

13. J. A. Schuller, S. Karaveli, T. Schiros, K. He, S. Yang, I. Kymissis, J. Shan and R. Zia, *Nat. Nanotechnol.*, 2013, **8**, 271-276.
14. M. Brotons-Gisbert, R. Proux, R. Picard, D. Andres-Penares, A. Branny, A. Molina-Sánchez, J. F. Sánchez-Royo and B. D. Gerardot, *Nat. Commun.*, 2019, **10**, 3913.
15. G. Wang, C. Robert, M. M. Glazov, F. Cadiz, E. Courtade, T. Amand, D. Lagarde, T. Taniguchi, K. Watanabe, B. Urbaszek and X. Marie, *Phys. Rev. Lett.*, 2017, **119**, 047401.
16. K.-z. Du, Q. Tu, X. Zhang, Q. Han, J. Liu, S. Zauscher and D. B. Mitzi, *Inorg. Chem.*, 2017, **56**, 9291-9302.
17. M. Cinquino, A. Fieramosca, R. Mastria, L. Polimeno, A. Moliterni, V. Olieric, N. Matsugaki, R. Panico, M. De Giorgi, G. Gigli, C. Giannini, A. Rizzo, D. Sanvitto and L. De Marco, *Adv. Mater.*, 2021, **33**, 2102326.
18. A. Fieramosca, L. De Marco, M. Passoni, L. Polimeno, A. Rizzo, B. L. T. Rosa, G. Cruciani, L. Dominici, M. De Giorgi, G. Gigli, L. C. Andreani, D. Gerace, D. Ballarini and D. Sanvitto, *ACS Photonics*, 2018, **5**, 4179-4185.
19. K. Xu, Z. Zou, W. Li, L. Zhang, M. Ge, T. Wang and W. Du, *Nano Lett.*, 2024, **24**, 3647-3653.
20. H.-H. Fang, J. Yang, S. Adjokatse, E. Tekelenburg, M. E. Kamminga, H. Duim, J. Ye, G. R. Blake, J. Even and M. A. Loi, *Adv. Funct. Mater.*, 2020, **30**, 1907979.
21. J. J. P. Thompson, M. Dyksik, P. Peksa, K. Posmyk, A. Joki, R. Perea-Causin, P. Erhart, M. Baranowski, M. A. Loi, P. Plochocka and E. Malic, *Adv. Energy Mater.*, 2024, **14**, 2304343.
22. K. Tanaka, T. Takahashi, T. Kondo, K. Umeda, K. Ema, T. Umebayashi, K. Asai, K. Uchida and

N. Miura, *Jpn. J. Appl. Phys.*, 2005, **44**, 5923.

23. M. Dyksik, H. Duim, D. K. Maude, M. Baranowski, M. A. Loi and P. Plochocka, *Sci. Adv.*, 2021, **7**, eabk0904.
24. C. Quarti, G. Giorgi, C. Katan, J. Even and M. Palummo, *Adv. Opt. Mater.*, 2024, **12**, 2202801.
25. G. Liu, C. Qiu, B. Tian, X. Pan, D. Ding, Y. Chen, C. Ren, T. He, Y. Shi, C. Su, Y. Li, Y. Gao and D. Fan, *ACS Appl. Electron. Mater.*, 2019, **1**, 2253-2259.
26. W. Paritmongkol, E. R. Powers, N. S. Dahod and W. A. Tisdale, *J. Phys. Chem. Lett.*, 2020, **11**, 8565-8572.
27. A. A. Koegel, E. M. Mozur, I. W. H. Oswald, N. H. Jalarvo, T. R. Prisk, M. Tyagi and J. R. Neilson, *J. Am. Chem. Soc.*, 2022, **144**, 1313-1322.
28. C. Qin, L. Xu, Z. Zhou, J. Song, S. Ma, Z. Jiao and Y. Jiang, *J. Mater. Chem. A*, 2022, **10**, 3069-3076.
29. X. Dong, M. Chen, R. Wang, Q. Ling, Z. Hu, H. Liu, Y. Xin, Y. Yang, J. Wang and Y. Liu, *Adv. Energy Mater.*, 2023, **13**, 2301006.
30. N. Marchal, E. Mosconi, G. García-Espejo, T. M. Almutairi, C. Quarti, D. Beljonne and F. De Angelis, *J. Phys. Chem. Lett.*, 2021, **12**, 2528-2535.
31. X. Tan, Q. Feng and G. Nan, *Mater. Horiz.*, 2024, **11**, 2248-2257.
32. C. G. Bailey, L. V. Gillan, M. Lee, N. Sloane, X. Liu, X. Hao, A. M. Soufiani and D. R. McCamey, *Adv. Funct. Mater.*, 2024, **34**, 2308095.
33. S. Li, X. Li, C. A. Kocoj, X. Ji, S. Yuan, E. C. Macropulos, C. C. Stoumpos, F. Xia, L. Mao, M. G. Kanatzidis and P. Guo, *Phys. Rev. Lett.*, 2022, **129**, 177401.
34. S. Zuri, A. Shapiro, L. Kronik and E. Lifshitz, *J. Phys. Chem. Lett.*, 2023, **14**, 4901-4907.

35. D. B. Straus, N. Iotov, M. R. Gau, Q. Zhao, P. J. Carroll and C. R. Kagan, *J. Phys. Chem. Lett.*, 2019, **10**, 1198-1205.

36. D. B. Straus and C. R. Kagan, *Annu. Rev. Phys. Chem.*, 2022, **73**, 403-428.

37. G. Kresse and J. Furthmüller, *Phys. Rev. B*, 1996, **54**, 11169-11186.

38. P. E. Blöchl, *Phys. Rev. B*, 1994, **50**, 17953-17979.

39. J. P. Perdew, K. Burke and M. Ernzerhof, *Phys. Rev. Lett.*, 1996, **77**, 3865-3868.

40. S. Grimme, *J. Comput. Chem.*, 2006, **27**, 1787-1799.

41. M. Gajdoš, K. Hummer, G. Kresse, J. Furthmüller and F. Bechstedt, *Phys. Rev. B*, 2006, **73**, 045112.

42. M. Marques, N. Maitra, F. Nogueira, E. K. U. Gross and A. Rubio, *Fundamentals of Time-Dependent Density Functional Theory*, Springer Science & Business Media, Berlin, 2012.

43. S. Refaely-Abramson, M. Jain, S. Sharifzadeh, J. B. Neaton and L. Kronik, *Phys. Rev. B*, 2015, **92**, 081204.

44. S. Refaely-Abramson, S. Sharifzadeh, N. Govind, J. Autschbach, J. B. Neaton, R. Baer and L. Kronik, *Phys. Rev. Lett.*, 2012, **109**, 226405.

45. D. Wing, J. B. Haber, R. Noff, B. Barker, D. A. Egger, A. Ramasubramaniam, S. G. Louie, J. B. Neaton and L. Kronik, *Phys. Rev. Mater.*, 2019, **3**, 064603.

46. J. Liu, G. Lu and X. Zhang, *J. Chem. Phys.*, 2023, **158**, 044116.

47. S. Wang, M. Dyksik, C. Lampe, M. Gramlich, D. K. Maude, M. Baranowski, A. S. Urban, P. Plochocka and A. Surrente, *Nano Lett.*, 2022, **22**, 7011-7019.

48. A. Shinde, P. K. Rajput, U. Makhija, R. Tanwar, P. Mandal and A. Nag, *Nano Lett.*, 2023, **23**, 6985-6993.

49. K. Posmyk, N. Zawadzka, K. Łucja, M. Dyksik, A. Surrente, D. K. Maude, T. Kazimierczuk, A.

Babiński, M. R. Molas, W. Bumrungsan, C. Chooseng, W. Paritmongkol, W. A. Tisdale, M. Baranowski and P. Plochocka, *J. Am. Chem. Soc.*, 2024, **146**, 4687-4694.

50. K. Posmyk, N. Zawadzka, M. Dyksik, A. Surrente, D. K. Maude, T. Kazimierczuk, A. Babiński, M. R. Molas, W. Paritmongkol, M. Mączka, W. A. Tisdale, P. Płochocka and M. Baranowski, *J. Phys. Chem. Lett.*, 2022, **13**, 4463-4469.
51. M. Gramlich, M. W. Swift, C. Lampe, J. L. Lyons, M. Döblinger, A. L. Efros, P. C. Sercel and A. S. Urban, *Adv. Sci.*, 2022, **9**, 2103013.
52. J. Hong, D. Prendergast and L. Z. Tan, *Nano Lett.*, 2021, **21**, 182-188.
53. B. Chen, R. Yu, G. Xing, Y. Wang, W. Wang, Y. Chen, X. Xu and Q. Zhao, *ACS Energy Lett.*, 2024, **9**, 226-242.
54. X. Ni, H. Li and J.-L. Brédas, *ACS Mater. Lett.*, 2024, **6**, 3436-3442.
55. W. Li, S. Giannini, C. Quarti, Z. Hou, O. V. Prezhdo and D. Beljonne, *J. Chem. Theory Comput.*, 2023, **19**, 9403-9415.
56. J. J. Geuchies, J. Klarbring, L. D. Virgilio, S. Fu, S. Qu, G. Liu, H. Wang, J. M. Frost, A. Walsh, M. Bonn and H. Kim, *Nano Lett.*, 2024, **24**, 8642-8649.
57. S. Tan, N. Zhou, Y. Chen, L. Li, G. Liu, P. Liu, C. Zhu, J. Lu, W. Sun, Q. Chen and H. Zhou, *Adv. Energy Mater.*, 2019, **9**, 1803024.
58. W. Li, Z. Hadjri, L. M. Devenica, J. Zhang, S. Liu, J. Hone, K. Watanabe, T. Taniguchi, A. Rubio and A. Srivastava, *Nat. Mater.*, 2023, **22**, 1478-1484.
59. L. Yu, K. Pistunova, J. Hu, K. Watanabe, T. Taniguchi and T. F. Heinz, *Nat. Mater.*, 2023, **22**, 1485-1491.
60. Z. Lian, D. Chen, L. Ma, Y. Meng, Y. Su, L. Yan, X. Huang, Q. Wu, X. Chen, M. Blei, T. Taniguchi,

K. Watanabe, S. Tongay, C. Zhang, Y.-T. Cui and S.-F. Shi, *Nat. Commun.*, 2023, **14**, 4604.

Data availability

The data that support the findings of this study are available from the corresponding author upon reasonable request.